

# Ultra-shallow DoF imaging using faced paraboloidal mirrors

Ryoichiro Nishi, Takahito Aoto, Norihiko Kawai, Tomokazu Sato,  
Yasuhiro Mukaigawa, Naokazu Yokoya

Graduate School of Information Science, Nara Institute of Science and Technology  
{nishi.ryoichiro.ne6, takahito-a, norihi-k, tomoka-s,  
mukaigawa, yokoya}@is.naist.jp

**Abstract.** We propose a new imaging method that achieves an ultra-shallow depth of field (DoF) to clearly visualize a particular depth in a 3-D scene. The key optical device consists of a pair of faced paraboloidal mirrors with holes around their vertexes. In the device, a lens-less image sensor is set at one side of their holes and an object is set at the opposite side. The characteristic of the device is that the shape of the point spread function varies depending on both the positions of the target 3-D point and the image sensor. By leveraging this characteristic, we reconstruct a clear image for a particular depth by solving a linear system involving position-dependent point spread functions. In experiments, we demonstrate the effectiveness of the proposed method using both simulation and an actually developed prototype imaging system.

## 1 Introduction

Shallow DoF (depth-of-field) imaging highlights a target in a photograph by de-focusing undesired objects that exist outside of a certain depth range. As an extreme condition, a microscope achieves ultra-shallow DoF imaging by putting a target object very close to the lens. In this case, the objects except for the tiny target, e.g. like a cell, are extremely blurred and we can see what we want to see by precisely adjusting the focus. Here, the range of DoF depends on the combination of the distance to a target and the aperture size. One problem is that the aperture size cannot be larger than the physical lens size. Although ultra large lenses are required to construct ultra shallow DoF imaging systems for standard size objects, it is almost impossible to produce such large lenses.

To solve this problem, a variety of synthetic aperture methods have been investigated and are classified into two categories: One physically captures images from multiple viewpoints using only standard cameras and the other virtually generates multi-view point images using cameras and some optical components. The former methods use a moving camera [1] or a multiple camera array system [2, 3]. Although they can widen the aperture using multi-view images taken from different viewpoints and synthesize full resolution images, they require time consuming camera calibration, or complex multi-camera devices. In the latter category, a micro lens array [4–6], mask [7, 8], and a micro mirror array [9–11] have

been employed to adjust the DoF. Since the aperture size in the systems cannot exceed that of the original camera lens equipped in their systems, it is practically difficult for these methods to achieve shallower DoF. As another method in the latter category, Tagawa et al. [12] proposed a specially designed polyhedral mirror called “turtleback reflector”, which can possibly achieve infinite-size aperture by reflecting light rays on mirrors arranged on a hemisphere placed in front of a camera. Although this optical system achieves the ultra-shallow DoF imaging, the resolution of the synthesized image is quite low because all images captured by multiple virtual cameras are recorded as one image in reality.

Another related approach is a confocal imaging one which highlights a specific 3-D point on a target by setting both the optical center of a camera and a point light source at the focus of a lens [13–15]. In the systems based on this approach, a half-mirror enables to set them at the same focus position. Since the systems cannot highlight all the positions on the target at the same time, they physically has to scan the target while changing the highlighted positions to reconstruct the complete image. In addition, since the systems can highlight only the target point within the DoF which are determined by the physical lens size, the size of the target object is still limited by available lenses.

In this paper, we propose a novel imaging device that consists of a pair of faced paraboloidal mirrors for achieving ultra-shallow DoF imaging. Such a device has first been developed for displaying 3D objects and is called “Mirage” [16]. This device is, for example, used for an interactive display [17]. In this study, we leverage this device to capture a cross-sectional image for a specific depth of a 3-D object. To the best of our knowledge, this study is the first one to use the paraboloidal mirrors-based device as an imaging device. The proposed system achieves much larger Numerical Aperture (NA) than those of existing lens-based camera systems, and has capability to handle larger size of objects than conventional microscope systems, while preserving the original image resolution of an image sensor.

## 2 Device for ultra shallow DoF imaging

This section introduces the proposed ultra shallow DoF imaging device that can capture a specific layer of an object that consists of multiple layers. Figures 1 and 2 show the developed prototype system of the proposed imaging device and its internal structure. The proposed imaging device consists of a pair of same shaped paraboloidal mirrors whose vertex and focal point correspond with each other and has holes at the vertexes of the paraboloidal mirrors for setting an image sensor without a lens at one side and a target object at the other side. It should be noted that paraboloidal mirrors have a feature that light rays from the focal point of a paraboloidal mirror become parallel after reflecting at the mirror and parallel light rays gather at the focal point after reflecting at the mirror as shown in Figs. 3(a) and (b). Therefore, light rays from an object at the focal point of an upper paraboloidal mirror gather at an image sensor at the focal point of the lower one. Here, since the direct light rays from the object to

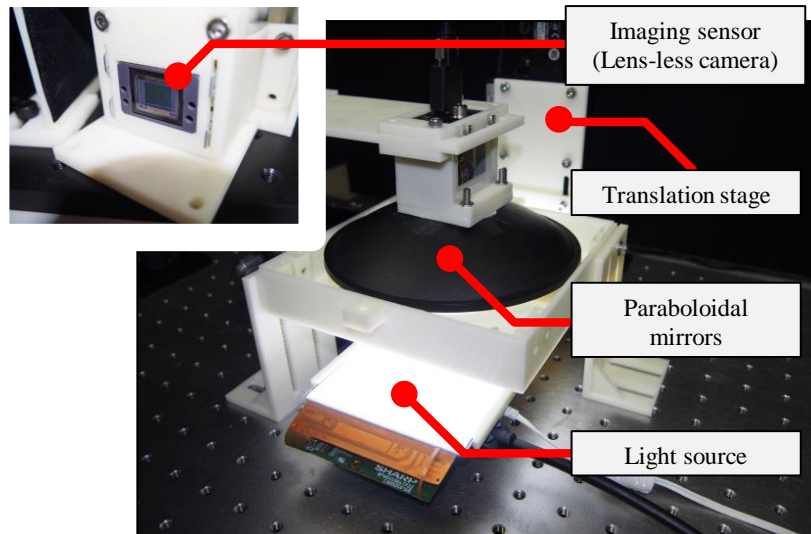


Fig. 1. Our prototype system.

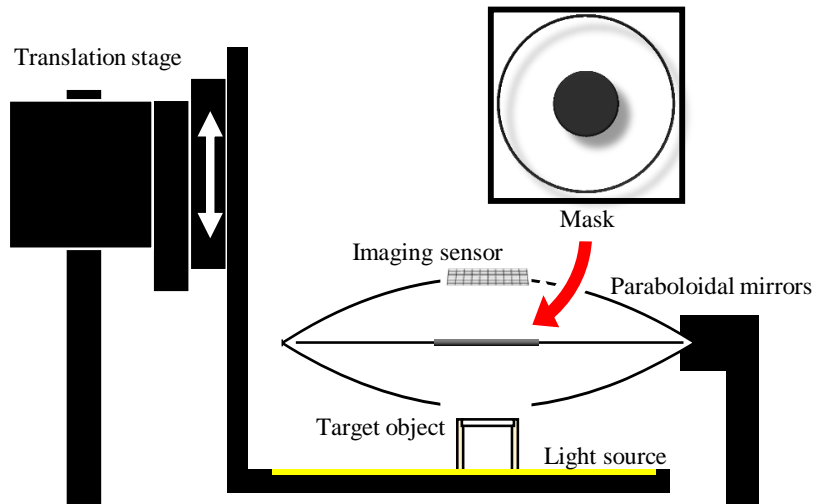


Fig. 2. Internal structure of prototype system.

the image sensor disturb the visualization of an internal layer, a thin mask is placed at the center of the proposed device for light rays from the object not to directly reach the image sensor as shown in Fig. 2. In addition, if an object moves from the focal point in the direction perpendicular to the image sensor plane (referred to as depth direction), light rays from the object do not gather

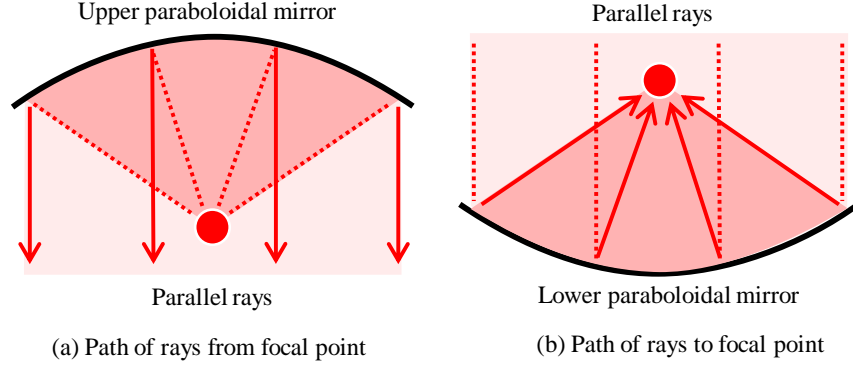


Fig. 3. Path of light rays in paraboloidal mirrors.

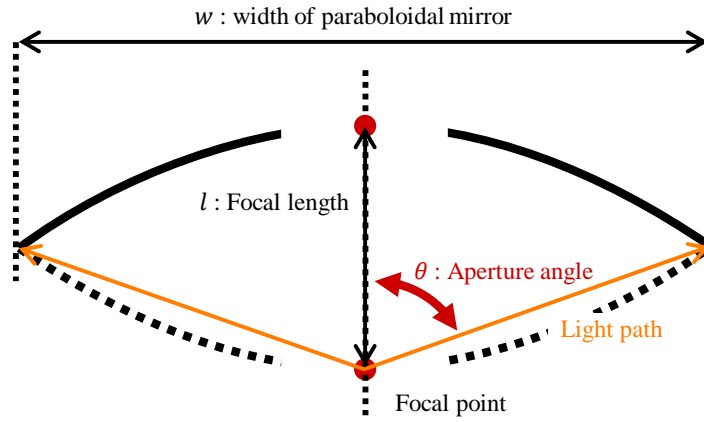


Fig. 4. Aperture angle in our system.

at the image sensor, resulting in generating a blurred image. Therefore, we can visualize only a specific layer that exists at the focal depth.

Here, we discuss the Numerical Aperture (NA) of the proposed imaging device. The range of the NA is  $[0, 1]$  and the DoF gets shallower as the NA gets higher. The NA is defined in general as follows:

$$NA = n \sin \theta, \quad (1)$$

where  $n$  is the index of refraction of the medium between a target object and an image sensor. In our case,  $n = 1.0$  because the medium is the air.  $\theta$  is the aperture angle which means the maximum angle between the optical axis and available light rays as shown in Fig. 4. We can calculate  $\sin \theta$  using the width  $w$

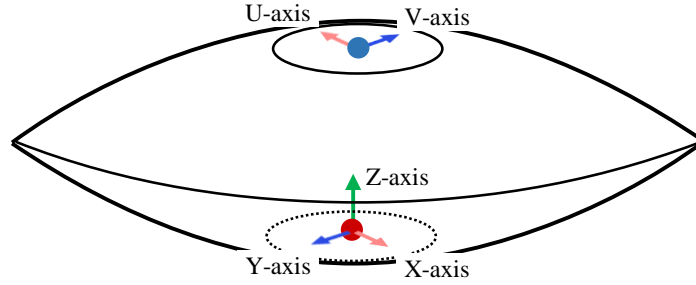


**Fig. 5.** Definition of coordinate systems.

and focal length  $l$  of the paraboloidal mirror as follows.

$$\sin \theta = \frac{\frac{w}{2}}{\sqrt{\left(\frac{w}{2}\right)^2 + \left(\frac{l}{2}\right)^2}}. \quad (2)$$

Here, since the expression of the paraboloidal mirror where  $y = 0$  in the coordinate system as shown in Fig. 5 is expressed as  $x^2 = 4lz$ , the relationship between the width  $w$  and the focal length  $l$  can be calculated from the following equation.

$$\left(\frac{w}{2}\right)^2 = 4l \left(\frac{l}{2}\right). \quad (3)$$

By replacing  $w$  with  $l$ , the NA of the proposed device is calculated as follows:

$$NA = \sin \theta = \frac{\sqrt{2}l}{\sqrt{2l^2 + \frac{l^2}{4}}} = \frac{2\sqrt{2}}{3} \simeq 0.94. \quad (4)$$

It should be noted here that the NA of the proposed device is a constant even if the scale of the paraboloidal mirror changes because the NA does not depend on the focal length and width of the paraboloidal mirror as indicated in Eq. (4).

Table 1 shows the comparison of the NAs of the proposed device and various commercial lenses. In this table, we calculated approximate NAs from F numbers using the following equation

$$NA = \frac{1}{2F} \quad (5)$$

From the table, we can confirm that the NA of the proposed device is much larger than those of various camera lenses and has competitive performance with objective lenses of microscopes. It should be noted that our system can handle relatively larger objects without constructing an ultra-large lens system which is practically almost impossible.

**Table 1.** Comparison of Numerical Aperture of various lenses.

NA	Lens type	Trade name
0.94	Mirror lens	Our approach
0.85	Objective lens (microsocpe)	WRAYMER GLF-ACH60X
0.59	Large aperture lens	HandeVision IBELUX 0.85/40MM
0.53	Fixed focal length lens	SCHNEIDER F0.95 Fast C-Mount Lens
0.36	Large aperture lens	Canon EF35mm F1.4L II USM

For the proposed device, depth of field  $d$  can be determined geometrically as follows:

$$d = d_{far} - d_{near}, \quad (6)$$

where  $d_{near}$  and  $d_{far}$  are distances from the image sensor to the nearest and farthest points that are in focus, respectively, and are calculated as follows:

$$d_{near} = \frac{l^2}{l + 2Fc}, \quad (7)$$

$$d_{far} = \frac{l^2}{l - 2Fc}, \quad (8)$$

where  $c$  is the size of a circle of confusion, which is the size of a pixel of an image sensor. For example, when  $c$  is  $0.01 \text{ mm}$ ,  $l$  is  $100 \text{ mm}$ , and the  $F$  number is  $0.53$  (i.e.,  $NA$  is  $0.94$ ), depth of field  $d$  becomes  $0.0212 \text{ mm}$ .

### 3 Experiments

In experiments, first, in order to check the raw performance of the proposed imaging device, the effect of geometric aberration is evaluated by measuring PSFs (point spread functions) which vary depending on the 3-D position of a target point, using a simulation environment. Layered real-images are then captured using a prototype imaging device and compared with images captured by a conventional lens-based camera device which has large  $NA$  in order to show the feasibility and the advantage of the proposed device. In addition to these two basic experiments for the proposed device, we further show the possibility to remove blurs on captured images using measured PSFs.

#### 3.1 Characteristic of faced paraboloidal mirror-based imaging device

The shape of the PSF, which is a response of an impulse input from a point light source, varies depending on the 3-D position of the point light source placed

in the proposed device. In order to analyze the characteristic of the proposed device, shapes of PSFs for different light source positions in the proposed imaging device are measured in a simulation environment. Experimental setting in this simulation is as follows: Focal length  $p$  is set to 65 mm. Width  $w$  of the mirror device is determined as 184 mm from Eq. (3). An imaging device ( $20 \text{ mm} \times 20 \text{ mm}$ ,  $201 \times 201$  pixels) is fixed at one of the two vertex positions. While moving the position of a point light source, we observed shapes of PSFs by this imaging device.

Figures 6 and 7 show the PSFs captured on the image plane  $(U, V)$  while moving a light source along the  $Z$  axis and  $X$  axis shown in Fig. 5, respectively. Since the proposed imaging device is rotationally symmetric, we can know the characteristic of the device using these two axes. From these figures, we can see that the shape of PSF drastically changes when the light source moves along  $Z$  axis as shown in Fig. 6, while the change of the PSF along  $X$  axis is comparatively moderate as shown in Fig. 7. This indicates that the object moving along  $Z$  axis from the vertex position immediately blurs, in contrast to the case for  $X$  direction. From this simulation, we can confirm the desirable characteristic of the proposed device for achieving ultra-shallow DoF imaging.

### 3.2 Ultra shallow DoF imaging using prototype

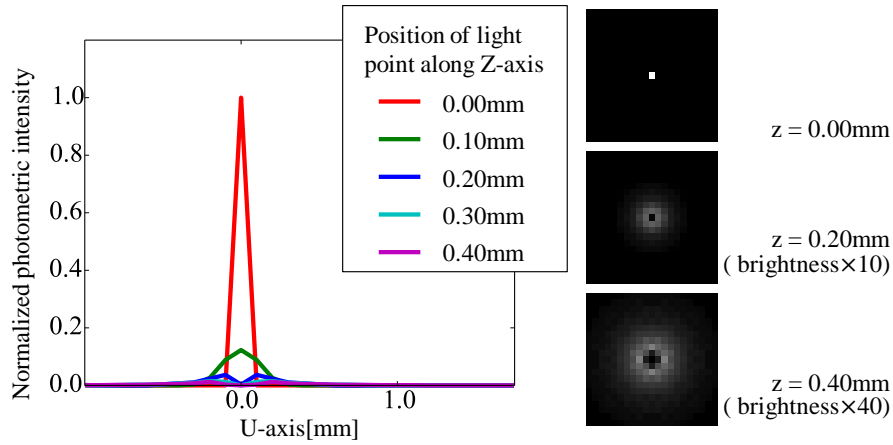
We have constructed the prototype device shown in Fig. 1. In this device, Point Grey Grasshopper2 ( $1,384 \times 1,036$  pixels, CCD) without a lens is employed as the image sensor and fixed at the vertex of the upper paraboloidal mirror. A target object is set at the vertex of the lower paraboloidal mirror and its depth can be adjusted by using a translation stage as shown in Fig. 2.

Figure 8 shows target objects 1 to 3 in this experiment which consist of two layered flat surfaces which are transparent films with 0.1mm thickness where different images are printed. The sizes of surfaces are  $20 \text{ mm} \times 20 \text{ mm}$  and two layers are separated with 1.2mm empty gap.

Target 1 and 2 shown in Fig. 8(a),(b) are layered objects where a grid mask texture which contains high frequency component is commonly used as upper layer images and low and high frequency textures are used for lower layer images respectively. Target 3 (Fig. 8(c)) has low frequency texture image for upper layer and high frequency texture image for lower layer where lower layer is almost completely blinded with upper layer in a standard camera image.

Figures 9 to 11(a) show images captured by the camera (Grasshopper2) with a small DoF lens (Schneider Fast C-Mount Lens, 17mm FL,  $F=0.95$  ( $NA=0.53$ )) for different height positions  $Z$  of the target objects. As we can see in these figures, the lower layer images are partially blinded by the grid patterns for the target 1 and 2, and the lower image is completely blinded for the target 3 even when we have employed relatively shallow DoF lens.

In contrast to this, one of two layer images is largely blurred by the proposed device not depending on the combination of low and high frequency textures, and the other layer image is focused as shown in Figs. 9 to 11(b). Even for the target 3, the characters behind the upper layer image are readable as shown in Fig.



**Fig. 6.** Observed PSFs for different  $Z$  positions of a point light source with  $X = 0$ . (left: slice of PSF with  $V = 0$ , right: cropped PSF image)

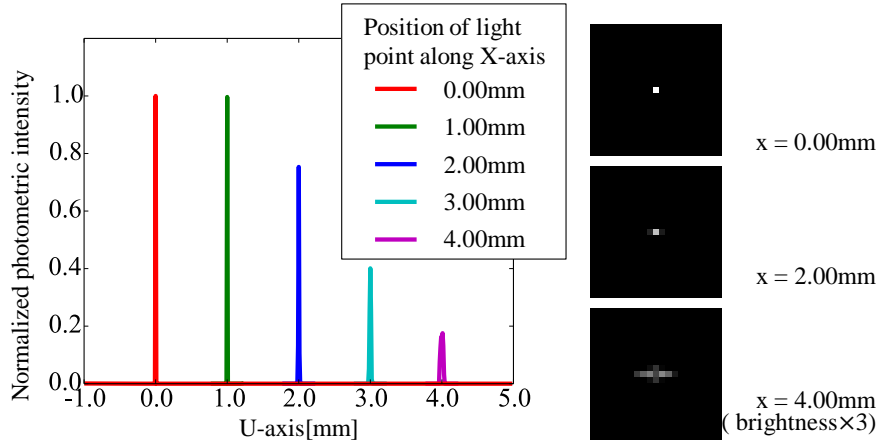


**Fig. 7.** Observed PSFs for different  $X$  positions of a point light source with  $Z = 0$ . (left: slice of PSF with  $V = 0$ , right: cropped PSF image)

11(b). By this comparison, we can conclude that our system can achieve much shallower DoF imaging than the conventional lens-based system. However, we also confirmed that the proposed device still has two problems: (1) The images captured by the proposed device blur in the peripheral regions more than the conventional lens, which means that the proposed device has worse geometric aberration than conventional lenses, and (2) textures from the other non-focused layer still remain a little in the captured images.

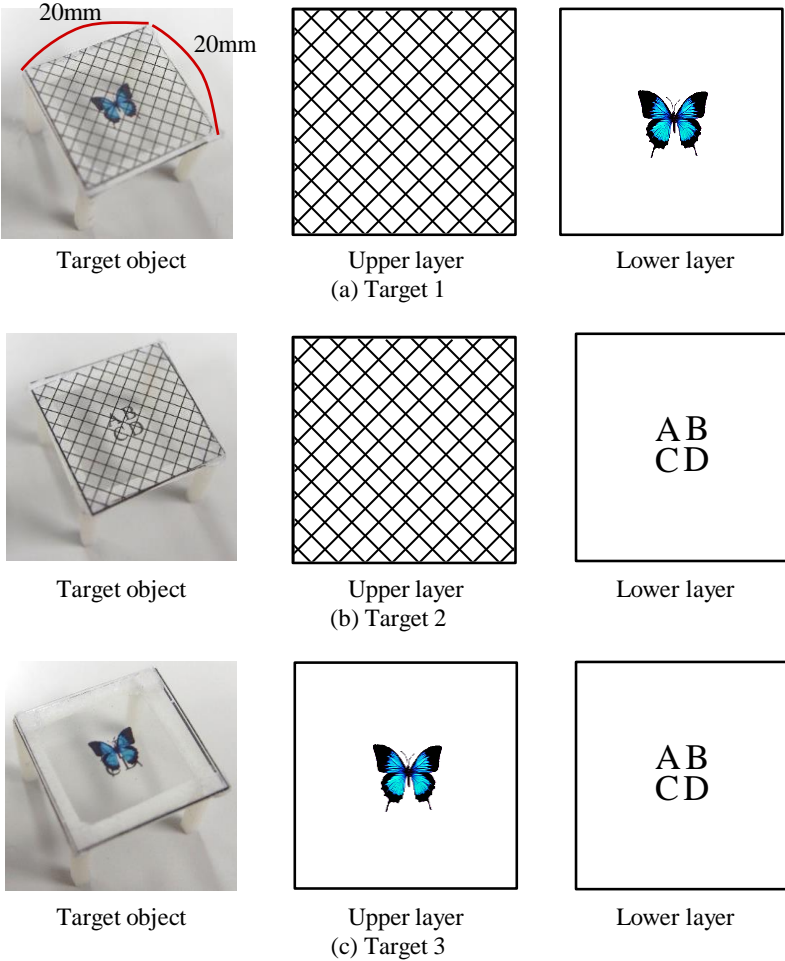
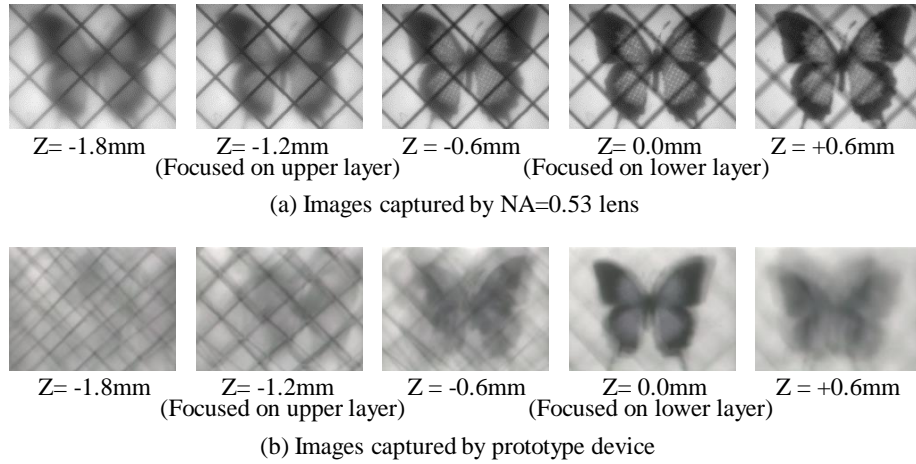


Fig. 8. Target objects and texture images for layers.

### 3.3 Reconstruction of layer images using PSFs

As described in the previous section, the proposed device has the weakness about the blurring effect caused by the aberration and the influences from other layers. In order to confirm the future possibility to overcome this weakness, here we simply deblur the observed images using measured PSFs by the following manner.

In the proposed system, theoretically, vectorized observed image  $\mathbf{o}$  can be represented as the weighted sum of the multiplication of intensity  $w_k$  of the  $k$ -th point light source and vectorized PSF  $\mathbf{p}_k$  for the light-source position  $k$  in the



**Fig. 9.** Experimental results for target 1.

device as follows:

$$\mathbf{o} = \sum_k w_k \mathbf{p}_k, \quad (9)$$

where we ignore occlusion effects for simplicity. Here, if  $\mathbf{p}_k$  is given by the calibration as shown in the first experiment and we have multiple observed images  $\mathbf{o}$  with different depths, we can easily estimate  $w_k$ , which means that the aberration is suppressed and the captured images are decomposed into ones for respective layers, by minimizing the sum of error  $\|\mathbf{o} - \sum_k w_k \mathbf{p}_k\|^2$  subject to  $w_k \geq 0$  with convex optimization [18].

In this experiment, we have tested this method using the same device configuration with the second experiment in the simulated environment. The target object here consists of two layered films with 0.5 mm gap where different images are printed as in Fig. 12, which is more severe situation with narrower gap than that in the previous experiment. For this target, we have captured five images by moving the height of the object (focus point of the device) with 0.25mm interval as shown in this figure.

Figure 13 shows the effect of decomposition. In this figure, (a) shows original layer images, (b) shows the images captured by focusing on upper and lower layers, (c) shows the decomposed results from the two images of (b), and (d) shows the decomposed results from all the five images. As shown in (b), even if the focus point is precisely adjusted to the position where target layer exists, the effect from the other layer image cannot be avoided, resulting blur effect in this severe situation as similar to the results in the previous experiment. As shown in (c) and (d) in Fig. 13, using this comparatively simple decomposition algorithm, the blurs were successfully reduced even by the two images, and were almost completely removed by the five images.

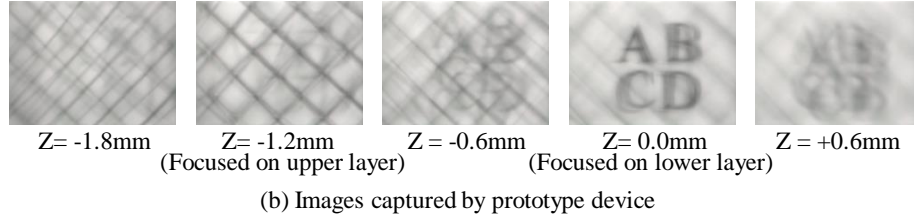
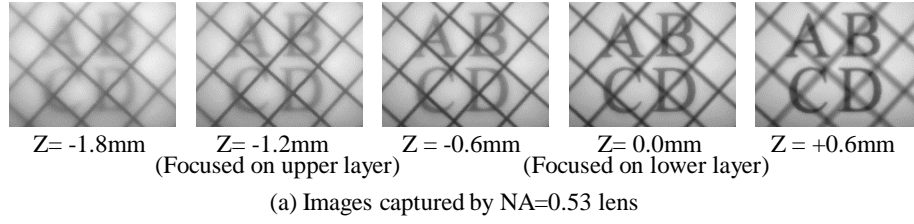


**Fig. 10.** Experimental results for target 2.

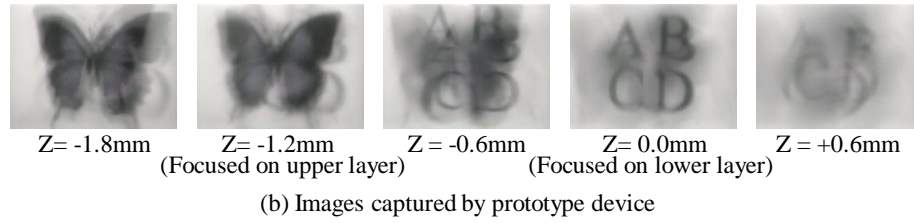
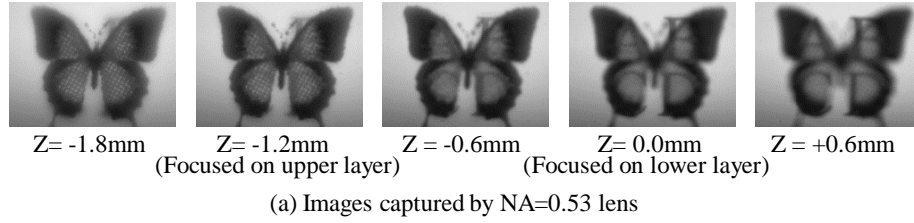


**Fig. 11.** Experimental results for target 3.

On the other hand, in the real world, to decompose images captured by the prototype system, we need to know a PSF for each spatial position in a target scene. A straightforward way to measure the PSFs is to prepare a hole whose size is smaller than that of a circle of confusion and align it with each spatial point. However, it is almost infeasible to create such a small hole and align it with each position accurately without special and expensive devices. Therefore, we should develop a method to measure PSFs that is an alternative to the way above in the future.

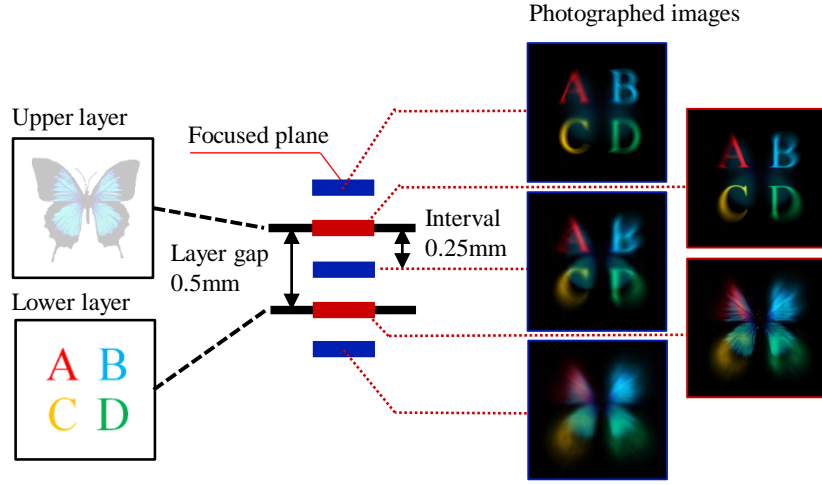


Fig. 12. Texture images for layers and captured input images for different height po-

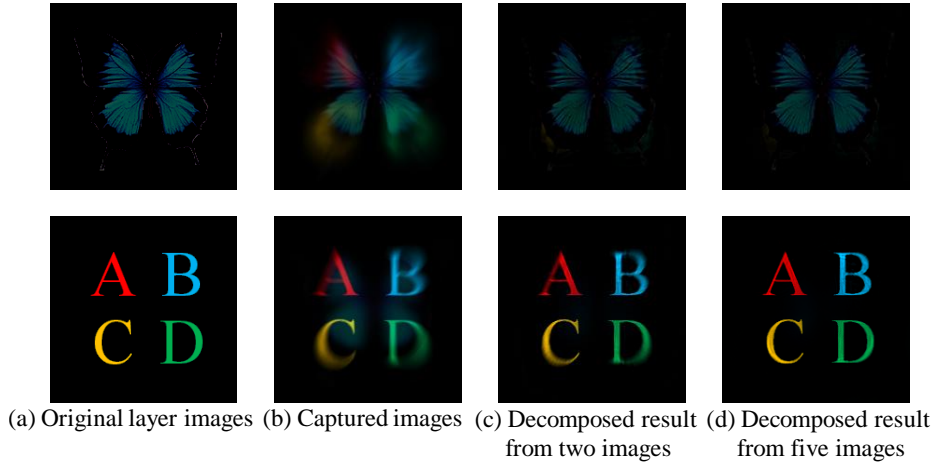


Fig. 13. Effect of decomposition. Top and bottom row show upper and lower layer images, respectively.

## 4 Conclusion

This paper has proposed an ultra-shallow DoF imaging method using faced paraboloidal mirrors that can visualize a specific depth. We constructed a prototype system and confirmed the proposed device can capture a specific depth using objects with two layers clearer than a small DoF lens. In the experiment using a simulation environment, we analyzed the characteristic of the proposed

device, and we showed that the proposed system also can suppress the aberration and decompose layered images into clear ones using measured PSFs. In future work, we will develop a decomposition method considering occlusions and apply it to images captured by the developed prototype system.

**Acknowledgement.** This work was supported by JSPS Grant-in-Aid for Research Activity Start-up Grant Number 16H06982.

## References

1. Levoy, M., and Hanrahan, P., Light field rendering. Proc. SIGGRAPH, pp. 31-42, 1996.
2. Vaish, V., Wilburn, B., Joshi, N., and Levoy, M., Using plane + parallax for calibrating dense camera arrays. Proc. CVPR, Vol. 1, pp. I-2-I-9, 2004.
3. Wilburn, B., Joshi, N., Vaish, V., Talvala, E.V., Antunez, E., Barth, A., Adams, A., Horowitz, M., and Levoy, M., High performance imaging using large camera array. ACM Trans. on Graph., Vol. 24, No. 3, pp. 765-776, 2005.
4. Adelson, E. H., and Wang, J. Y. A., Single lens stereo with a plenoptic camera. IEEE Trans. on PAMI, pp. 99-106, 1992.
5. Ng, R., Levoy, M., Bredif, M., Duval, G., Horowitz, M., Hanrahan, P., Light field photography with a hand-held plenoptic camera. Proc CTSR, Vol. 2, No. 11, pp. 111, 2005.
6. Cossairt, O., Nayar, S., and Ramamoorthi, R., Light field transfer: global illumination between real and synthetic objects. ACM Trans. on Graph., Vol. 27, No. 3, pp. 57:1-57:6, 2008.
7. Veeraraghavan, A., Raskar, R., Agrawal, A., Mohan, A., and Tumblin, J., Dappled photography: mask enhanced cameras for heterodyned light fields and coded aperture refocusing. ACM Trans. on Graph., Vol. 26, No. 3, pp 69-76, 2007.
8. Liang, C., Lin, T., Wong, B., Liu, C., and Chen, H. H., Programmable aperture photography: multiplexed light field acquisition. ACM Trans. on Graph., Vol.27, No.5, pp. 55-1-55-10, 2008.
9. Unger, J., Wenger, A., Hawkins, T., Gardner, A., and Debevec, P., Capturing and rendering with incident light Fields. Proc. EGSR, pp. 141-149, 2003.
10. Lanman, D., Crispell, D., Wachs, M., and Taubin, G., Spherical catadioptric arrays: construction, multi-view geometry, and calibration. Proc. 3DPVT, pp. 81-88, 2006.
11. Levoy, M., Chen, B., Vaish, V., Horowitz, M., McDowall, I., and Bolas, M., synthetic aperture confocal imaging. Proc. SIGGRAPH, pp. 825-834, 2004.
12. Tagawa, S., Mukaigawa, Y., Kim, J., Raskar, R., Matsushita, Y., and Yagi, Y., Hemispherical confocal imaging. IPSJ Trans. on CVA, Vol. 3, pp 222-235, 2011.
13. Minsky, M., Microscopy apparatus. US Patent 3013467, 1961.
14. White, J., G., Amos, W. B., and Fordham, M., An evaluation of confocal versus conventional imaging of biological structures by fluorescence light microscopy. JCB, Vol. 501, No. 1, pp. 41-48, 1987.
15. Tanaami, T., Otsuki, S., Tomosada, N., Kosugi, Y., Shimizu, M., and Ishida, H., High-speed 1-frame/ms scanning confocal microscope with a microlens and nipkow disks. APPLIED OPTICS, Vol. 41, No. 22, pp. 4704-4708, 2002.
16. Adhya, S., and Noé, J., A complete ray-trace analysis of the 'Mirage' toy. Proc. SPIE ETOP, pp. 966518-1-966518-7, 2007.

17. Butler, A., Hilliges, O., Izadi, S., Hodges, S., Molyneaux, D., Kim, D., and Kong, D., Vermeer: direct interaction with a 360° viewable 3D display. Proc. UIST, pp 569-576, 2011.
18. Gabay, D., and Mercier, B., A dual algorithm for the solution of nonlinear variational problems via finite-element approximations, Comput. Math. Appl., vol. 2, pp. 17-40, 1976.